PAPER • OPEN ACCESS

Multi-second magnetic coherence in a single domain spinor Bose–Einstein condensate

New Journal of Physics
The open access journal at the forefront of physics

Deutsche Physikalische Gesellschaft DPG
IOP Institute of Physics

Published in partnership with: Deutsche Physikalische Gesellschaft and the Institute of Physics

OPEN ACCESS

RECEIVED
4 September 2017

REVISED
21 February 2018

ACCEPTED FOR PUBLICATION
27 February 2018

PUBLISHED
2 May 2018

PAPER

Multi-second magnetic coherence in a single domain spinor Bose–Einstein condensate

Silvana Palacios[1,6], **Simon Coop**[1], **Pau Gomez**[1], **Thomas Vanderbruggen**[2], **Y. Natali Martinez de Escobar**[3], **Martijn Jasperse**[4] **and Morgan W Mitchell**[1,5]

[1] ICFO—Institut de Ciencies Fotoniques, The Barcelona Institute of Science and Technology, E-08860 Castelldefels (Barcelona), Spain
[2] Koheron, Centre scientifique d'Orsay, Batiment 503, F-91400 Orsay, France
[3] Lone Star College, University Park, Chemistry and Physics Department, Houston, TX 77070, United States of America
[4] School of Physics, The University of Melbourne, Parkville, VIC 3010, Australia
[5] ICREA—Institució Catalana de Recerca i Estudis Avançats, E-08010 Barcelona, Spain
[6] Author to whom any correspondence should be addressed.

E-mail: silvana.palacios@icfo.es

Keywords: spinor condensate, Faraday probing, all-optical evaporation, magnetic coherence

Abstract

We describe a compact, robust and versatile system for studying the macroscopic spin dynamics in a spinor Bose–Einstein condensate. Condensates of ^{87}Rb are produced by all-optical evaporation in a 1560 nm optical dipole trap, using a non-standard loading sequence that employs an ancillary 1529 nm beam for partial compensation of the strong differential light-shift induced by the dipole trap itself. We use near-resonant Faraday rotation probing to non-destructively track the condensate magnetization, and demonstrate few-Larmor-cycle tracking with no detectable degradation of the spin polarization. In the ferromagnetic $F = 1$ ground state, we observe the spin orientation between atoms in the condensate is preserved, such that they precess all together like one large spin in the presence of a magnetic field. We characterize this dynamics in terms of the single-shot magnetic coherence times $\mathcal{T}_1$ and $\mathcal{T}_2^*$, and observe them to be of several seconds, limited only by the residence time of the atoms in the trap. At the densities used, this residence is restricted only by one-body losses set by the vacuum conditions.

1. Introduction

Spinor Bose–Einstein condensates (SBECs) are rich systems exhibiting coherent matter-wave behavior together with spin physics. When spatially extended, SBECs can show topological and kinematic features including vortices [1], skyrmions [2], Dirac monopoles [3] and magnon quasiparticles [4]. Much work has been dedicated to the emergence and dynamics of spin structures, including spontaneous symmetry breaking [5, 6], domain formation [7, 8] and spin texture development [9]. Less studied is spin dynamics in the so-called 'single-mode' (SM) regime, in which low density and tight confinement make spin structure energetically costly. In this regime all spin states share the same spatial mode and the single-mode approximation (SMA) is adopted to simplify the description of the system [10–12].

Prior work with SM SBECs has focused on condensates with zero mean spin polarization. For example, initial states with $m_F = 0$ give rise to twin Fock states [13], spin squeezing and entanglement [14–16], all relevant for quantum information and metrology. Studies with polarized SBECs in two-dimensional [17] and one-dimensional [18] traps show coherence times that increase as the geometry approaches the SM scenario. Indeed, one may surmise that for a polarized ferromagnetic SM SBEC only one magnetic domain is held and the magnetic coherence, or the expected value of the macroscopic spin, is degraded only by atom losses, this is, no depolarization mechanism will remain in the single domain SBEC (SD SBEC). This removes an important limitation of neutral atoms, which otherwise suffer from decoherence resulting from coupling of their internal and external degrees of freedom [19]. Decoherence is the most significant obstacle for applications in quantum

information science [20–22] and therefore demonstrating long coherence and scalability of the quantum system, make the SD SBEC interesting for long-lived entanglement [23–25], spin-squeezing [14, 26], and studies of quantum non-locality [27]. Additionally, one can profit from the small size of the condensate for applications like high-resolution magnetic sensing [28, 29].

Here we confirm the SD SBEC shows multi-second magnetic coherence, observing undetectably small polarization relaxation in a ferromagnetic SBEC. We create spinor condensates with 4×10^4 atoms in the $F = 1$ ferromagnetic manifold of ^{87}Rb which occupy a single spatial spin domain. Using non-destructive Faraday rotation probing we observe spin dynamics where the quadratic Zeeman effect modulates the Larmor precession. This dynamics occurs without dephasing, in contrast to similar experiments where the system breaks into different domains causing decoherence [18]. In our system only atom losses degrade the macroscopic spin polarization, giving a spin coherence time equal to the trap lifetime. At the used densities, the lifetime is set only by one-body losses. The trap lifetime time ≈8 s can in principle be extended with better vacuum conditions up to the three-body loss time ≈70 s.

This work is organized as follows: section 2 describes our experimental approach to form a spinor condensate in a polarized state. It is comprised of a minimalist design of the apparatus an all-optical evaporation in an optical dipole trap (ODT). We also briefly describe our loading technique, which allows us to use the full available power of the ODT while also exploiting the large differential light-shift produced by the ODT to create an effective dark MOT.

In section 3 we give evidence the system is well described by the SMA. In section 4 we describe the Zeeman dynamics of an atomic ensemble in the presence of a magnetic field. In section 5 we describe the non-destructive Faraday rotation measurement implementation and characterization, which we employ to read out the spin state of the atoms. Finally in section 6 we show the spinor condensate is immune to most decoherence mechanisms which allows the spin state to remain coherent on the scale of seconds.

2. Apparatus and state preparation

As shown in figure 1, the vacuum system consists of an all-glass, 9-window enclosure (Octagonal BEC Cell 4, Precision Glassblowing) in which an ultimate pressure of 10^{-11} Torr can be maintained with a single pumping element (TiTan 25SVW, Gamma Vacuum). The glass cell is AR coated for 780 nm and 1560 nm to reach single-window transmission of 97% and 99% respectively. The ion pump is shielded with a high-permeability enclosure which reduces the magnetic field produced by its magnets by a factor of ∼400, such that the field around the glass cell is mainly due to the earth's magnetic field. ^{87}Rb is deposited in the chamber by sublimating rubidium from dispensers mounted inside (Alvasource-3-Rb87-C, Alvatec). Following activation of the dispensers the pressure rises to 2×10^{-10} Torr, which is the typical pressure of the experiment.

The laser system is built up around a single 'master laser'—a low noise, narrow linewidth laser that serves as a frequency reference for offset locking of the other lasers. The master laser is a 1560 nm fiber laser (Koheras Adjustik, NKT Photonics) amplified by an erbium-doped fiber amplifier to a maximum power of 3 W (Boostik, NKT Photonics), it is frequency-doubled in a periodically poled $LiNbO_3$ (PPLN) crystal of 50 mm length. The output at 780 nm has a maximum power of 170 mW and Voigt linewidth of about 4.75(6) kHz[7]. The master laser is locked 80 MHz to the blue side of the $|F = 2\rangle \rightarrow |F' = 3\rangle$ cooling transition (see figure 2) using modulation transfer spectroscopy [31]. The cooling and repumper lasers ('slave lasers') are extended-cavity diode lasers (Toptica) which are offset locked to the master laser using an optical phase-locked loop, as described in [32], where the ultrafast photodiode is a PIN receiver (PT10GC, Bookham) and the digital phase-frequency-discriminator chip is an ADF4110 (Analog Devices) in the case of the cooler and an ADF41020 for the repumper. The chips are interfaced with a micro-controller that allows us to re-program the loops during the experiment, thereby tuning the frequency of the slave laser.

In the glass cell, a 3D magneto-optical trap (MOT) is formed with a gradient field of 11.2 G cm^{-1}, generated by anti-Helmholtz coils mounted around the cell along the z axis. The bias field is compensated with three pairs of Helmholtz coils in each axis. The six, circularly polarized beams of the MOT have waists of 1 cm (propagating along $\pm x$ and $\pm z$ directions) or 0.5 cm (propagating along the $\pm y$ direction). Each beam contains both cooling and re-pumping light with maximum intensities of 14 mW cm^{-2} and 0.3 mW cm^{-2}, respectively. The cooler beam is 15 MHz red detuned from the $|F = 2\rangle \rightarrow |F' = 3\rangle$ cooling transition and the repumper is resonant with the $|F = 1\rangle \rightarrow |F' = 2\rangle$ transition. The steady state number of atoms in the MOT is 10^8 atoms at 200 μK.

[7] The linewidth was estimated from the measurement of the linewidth of the 1560 nm laser in a self-heterodyne interferometer with a 0.5 ms delay line. The analysis assumes the model proposed in [30] where the noise is modeled by white noise plus a $1/f$ component, which is due to thermal fluctuations. The first source of noise gives a Lorentzian character to the linewidth whereas the second one is Gaussian to good approximation. The convolution of both contributions results in a Voigt profile.

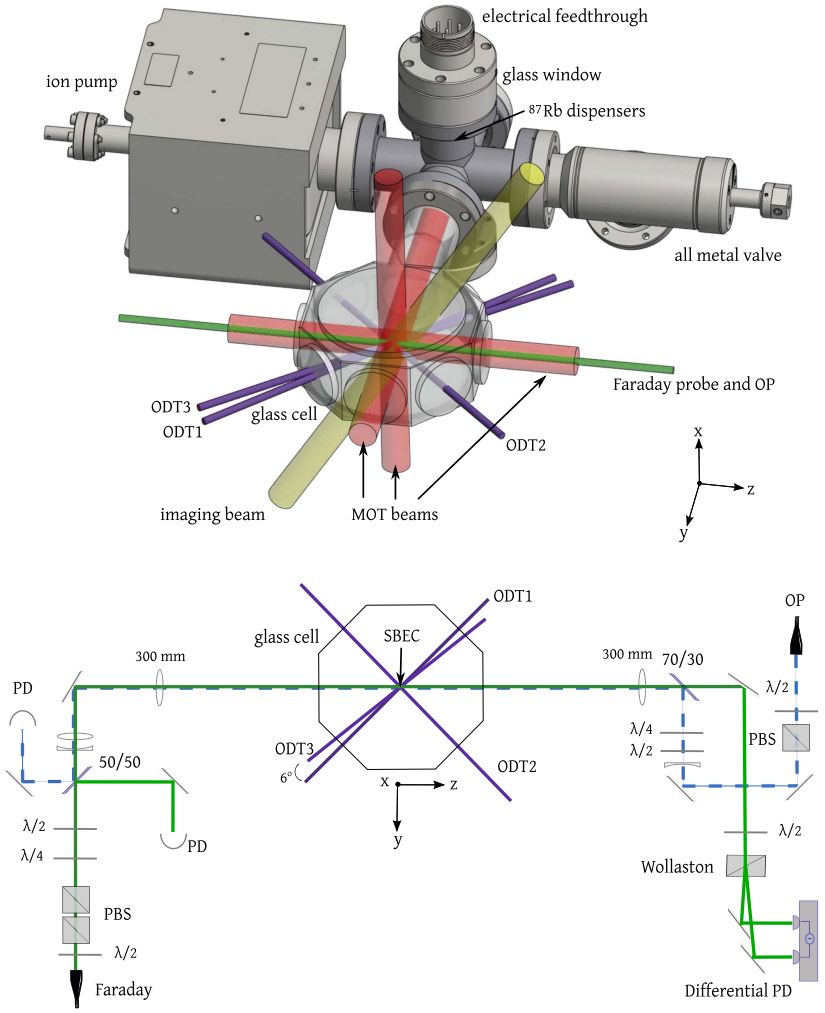

Figure 1. *Experimental setup*. (Above) General setup of the experiment to form a spinor condensate: from ^{87}Rb in a glass cell at room temperature we form a 3D MOT and transfer to and ODT where we perform all-optical evaporation. (below) Detailed setup to polarize the atoms and perform Faraday rotation measurements of the spin state. Continuous green lines represent the Faraday beam and dashed blue lines the optical pumping beam.

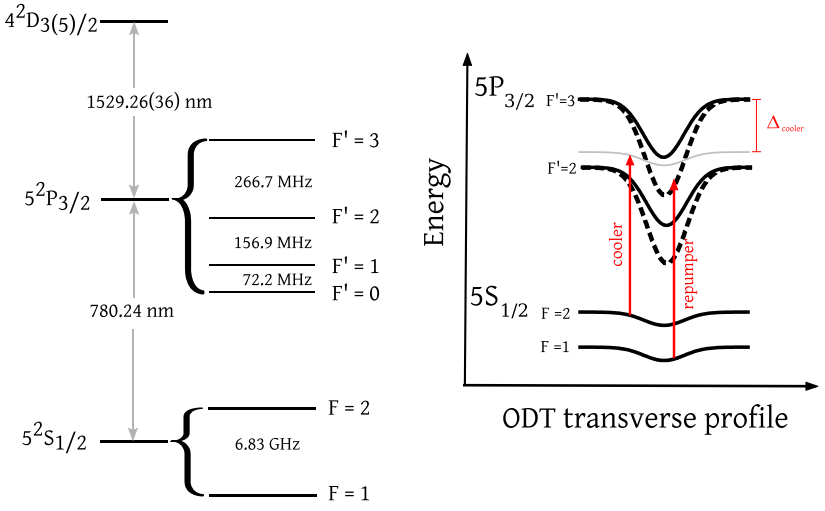

Figure 2. *Energy levels*. (Left) Relevant energy levels of ^{87}Rb in free space. (right) Illustration of differential light-shift as a function of the position in the optical dipole trap. Detuning of the laser is defined as $2\pi\,\Delta \equiv \omega_{\text{laser}} - (\omega_{F'} - \omega_F)$ thus positive values of Δ indicate blue detunings from the transition. Gray line indicates the detuning of the cooling beam. Dashed lines indicate the light-shift at full power of ODT1 with no compensation beam present, whereas continuous lines indicate the light-shift when the trap is partially compensated with the 1529.22 nm beam.

From the 3D MOT, the atoms are transferred to an ODT, formed at different stages of the experiment by up to three ODT beams. Each beam is linearly polarized, with wavelength 1560 nm and Gaussian spatial profile. ODT1 is focused to a waist of 45 μm at the center of the MOT, with maximum power of 11 W and is vertically polarized. ODT2 and ODT3 have waists 65 μm and horizontal polarization with maximum powers 10 W and 7 W respectively. ODT1 and ODT2 propagate along the diagonals in the y–z plane, with ODT3 at a 6° angle relative to ODT1 (figure 1). Acousto-optic modulators are used to shift ODT2 (ODT3) by −40 MHz (+40 MHz) relative to ODT1, to avoid spatial interference, as well as for power stabilization which is critical for proper evaporation control. In addition, a 'compensation' beam at 1529.22 nm with up to 6 mW of power, mode-matched to ODT1 but of orthogonal linear polarization, can be introduced.

Because the wavelength of the ODT is close to the $5P_{3/2}$–4D transitions of ^{87}Rb (1529 nm), the ac-Stark shift of the excited state $5P_{3/2}$ is much stronger than that of the ground state $5S_{1/2}$, as first reported by [33–35]. The ratio of these light-shifts is about 47, corresponding to the ratio of the scalar polarizabilities of the excited state and ground state. As a result, an intensity-dependent differential light-shift is induced on the D_2 line within the ODT, giving the cooler and repumper lasers spatially dependent detunings (see figure 2). We exploit this fact to form an effective dark MOT similar to that described in [33, 34, 36–38]: the atoms at the bottom of the potential are very unlikely to be re-pumped back into the $F = 2$ manifold, and thus they accumulate in $F = 1$, avoiding light-assisted collisions and radiation trapping.

ODT1 at maximum power creates a differential light-shift of 312 MHz at beam center, which is larger than the unperturbed hyperfine splitting between the $|F' = 2\rangle$ and $|F' = 3\rangle$ states. As a result, it is not possible to simultaneously address the cooling transition with red detuning in all spatial regions of the MOT, as shown in figure 2. This constraint was also reported in [34], where it was accommodated by limiting the ODT power. Here, in contrast, we compensate the excess differential light-shift with a 1529.22 nm beam, which is blue detuned from the $5P_{3/2}$–4D transitions. The trap-center light-shift induced by the compensating beam in the $5P_{3/2}$ manifold ranges from 95 MHz to 109 MHz for the different $|F' = 3,\ m_F\rangle$ sublevels, computed by Floquet theory as in [39]. In the presence of both 1560 nm and the 1529.22 nm beams, the differential light-shift at the bottom of the trap is reduced to 210 MHz. With this conditions, we are able to load ODT1 at full power and simultaneously exploit the dark MOT technique.

In the partially compensated dipole trap a molasses phase is started: the magnetic field gradient is suddenly switched off, the cooling laser is further detuned to 255 MHz to the red of the unshifted $|F = 2\rangle \rightarrow |F' = 3\rangle$ transition, and thus 45 MHz red-detuned at the bottom of the trap. The power of the repumper is lowered by a factor of 2.5 without changing the frequency. This phase lasts 500 ms, limited by the lifetime of the cold-atom reservoir. This strategy allows us to load up to 7×10^6 atoms in $|F = 1\rangle$ at 50 μK into the dipole trap. Using the compensation beam therefore improves the maximum number of atoms loaded by a factor of three respect to the non-compensating strategy of the ODT1 at full power, and by a factor of two loading ODT1 at a lower power for which the differential light-shift does not exceed the excited-state hyperfine splitting.

After the ODT is loaded, the cooler and repumper beams are switched off and the power of the compensation beam adiabatically lowered. At the same time, a magnetic field of magnitude $B_z = 1$ G is applied along the z axis. At this field, the atoms are optically pumped into the $|F = 1,\ m_F = +1\rangle$ state using a beam (OP) resonant with the $|F = 1\rangle \rightarrow |F' = 1\rangle$ transition and propagating along the z axis with σ^+ polarization. We achieve 90% efficiency of pumping as confirmed by Stern–Gerlach imaging along the quantization axis defined by the magnetic field. To avoid the effects of the spatially dependent differential light-shift on the atoms distributed in the trap, the optical pumping is done with three 20 μs OP pulses during which the ODT1 is switched off. The pulses are separated by 10 ms intervals to allow the atoms to redistribute in the trap and avoid shadowing effects.

Following optical pumping the atoms are allowed to thermalize for 500 ms, after which the cloud is compressed in the longitudinal direction of ODT1 using ODT3. ODT3 boosts the collision rate without reducing the large collection volume. Forced all-optical evaporation in this two-beam trap is possible and efficient down to 2 μK. At that point the longitudinal frequency becomes insufficient to reach higher phase space densities. We employ an extra beam, ODT2, to provide extra compression at the end of the evaporation.

The evaporation sequence is as follows: starting with all the three beams at full power, we perform forced all-optical evaporation for 4 s, after which the system crosses the critical temperature T_c with about 10^5 atoms. The power of ODT2 is then increased for an additional 800 ms to compress the atoms, resulting in the formation of a pure condensate with typically 4×10^4 atoms. The relative populations do not change during the evaporation, as discussed in section 6 below. Our experimental approach is similar to that recently described in [38].

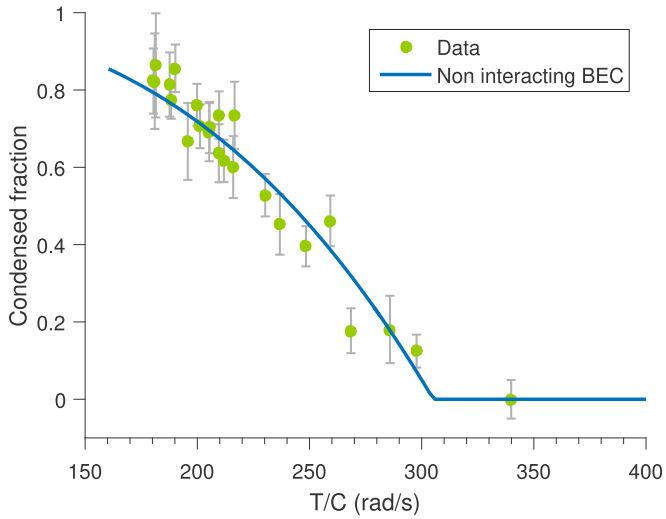

Figure 3. *Condensed fraction as a function of T/C.* The condensed fraction $c_F = N/N_{\rm tot}$ can be fitted by the model $c_F = \max\{1 - [T/(C\bar{\omega}_f)]^3, 0\}$, where the temperature $T = 54$ nK is constant and C is a function of the number of atoms $N_{\rm tot}$ (see text). In this measurement only $N_{\rm tot}$ varies and therefore $\bar{\omega}_f$ is the only free parameter, yielding to $\bar{\omega} = 2\pi \cdot 50(5)$ Hz.

3. Single spin domain

A natural measure of the spatial extent of the condensate is the Thomas–Fermi radius. The mean can be expressed in terms of fundamental constants, the number of condensed atoms N and the geometric mean oscillation frequency of the harmonic trap $\bar{\omega}$:

$$\bar{R}_{\rm TF} = \left(\frac{15Na_0\hbar^2}{M^2\bar{\omega}^2}\right)^{1/5} \tag{1}$$

where $a_0 = 5.38 \times 10^{-9}$ m is the scattering length and $M = 1.44 \times 10^{-25}$ kg the mass of one ^{87}Rb atom. The number of atoms is measured with time-of-flight absorption imaging for dense clouds [40].

The relative low atom number prevented direct measurement of the trap frequencies by parametric excitation. Instead we estimate $\bar{\omega}$ from the observable condensate fraction as follows: for N condensed atoms of a total $N_{\rm tot}$ atoms, the condensed fraction $c_F = N/N_{\rm tot}$ for non-interacting bosons obeys the relation: $c_F = \max[1 - (T/T_c)^3, 0]$, where the critical temperature in a harmonic trap is [41]:

$$T_c = \frac{\hbar\bar{\omega}}{k_{\rm B}}\left[\frac{N_{\rm tot}}{\zeta(3)}\right]^{1/3} \tag{2}$$

$k_{\rm B}$ is the Boltzmann constant and $\zeta(3) \approx 1.202$. Time-of-flight absorption imaging and a bi-modal fit give direct access to $N_{\rm tot}$, N (and thus c_F), as well as to T, which is found from the width of the thermal component. For fixed beam geometry and power, the trap frequencies are constant. The temperature is set by the potential depth at $T = 54(13)$ nK, independent of $N_{\rm tot}$. We can thus vary the critical temperature by changing only the number of atoms, through the duration of the ODT loading step. Figure 3 shows the condensed fraction as a function of T/C, where $C \equiv T_c/\bar{\omega}$. We fit the expected scaling of c_F where $\bar{\omega}$ is the only free parameter, to find $\bar{\omega} = 2\pi \cdot 50(5)$ Hz.

The mean Thomas–Fermi radius as given by equation (1) with $N = 4 \times 10^4$ atoms is then: $\bar{R}_{\rm TF} = 7.0(5)$ μm. From the geometry and power of the ODT beams the shape of the condensate is expected to be a spheroid, and thus large errors in what follows are not expected.

To gain some intuition about the expected spin variations in space the $R_{\rm TF}$ radius is compared to the spin healing length, which is defined as $\xi_s = \hbar/\sqrt{2M|c_1|n}$ [42, 43], where $c_1 = -2.39 \times 10^{-53}$ J m^3 characterizes the spin-dependent contact interaction [44], and n is the density. In our experimental conditions, $n = 2.7 \times 10^{13}$ cm^{-3} and $\xi_s = 7.7$ μm. With this parameters the density healing length is $\xi_n = \hbar/\sqrt{2Mc_0n} = 0.5$ μm for the spin-independent contact interaction parameter $c_0 \simeq 216|c_1|$. Since $\bar{R}_{\rm TF} \gg \xi_n$ the quantum pressure becomes relevant only near the boundary and therefore can be ignored, which implies the Thomas–Fermi approximation is reasonable. The spin healing length nevertheless, is such that $\xi_s \sim \bar{R}_{\rm TF}$, and the system is in an intermediate regime in regard to spin variations. Nonetheless, we observe no spin structure in TOF absorption images in the time scales of the condensate lifetime at the reported densities,

suggesting no domain formation occurs. In addition, we have observed long coherence times of the magnetization (section 6), which provides stronger evidence for this conclusion.

4. Excitation of spin oscillation and free oscillation

Within the SMA the order parameter can be written as $\hat{\mathbf{\Psi}}(\mathbf{r}) = \varphi(\mathbf{r})\hat{\mathbf{\Psi}}$, where $\varphi(\mathbf{r})$ defines the spatial mode which is common between all the spin states. We write the spinor as $\hat{\mathbf{\Psi}} \equiv (\hat{\psi}_{+1}, \hat{\psi}_0, \hat{\psi}_{-1})^T$, where $\hat{\psi}_{m_F}$ are the complex amplitudes describing the magnetic sublevels [11]. Single mode SBECs have been extensively used to study spin-mixing physics, in which collisional interactions produce interesting quantum dynamics and spin correlations [7, 8, 45–49]. These works study condensates with zero mean magnetic polarization, in a regime in which collisional and quadratic Zeeman energies compete [18, 46, 50]. In contrast, here we study the magnetic coherence properties of a low-density condensate, precisely to minimize the effect of collisional interactions.

A single atom exposed to a magnetic field $B_x(t)$ along the x direction experiences the spin Hamiltonian

$$\begin{aligned}\hat{H} &= \frac{g_J\mu_B}{4}B_x\hat{f}_x + \frac{g_J^2\mu_B^2}{16\Delta E_{hf}}B_x^2\hat{f}_x^2 + O(B_x^3)\\ &\equiv \hbar\omega_L\hat{f}_x + \hbar\omega_Q\hat{f}_x^2 + O(B_x^3),\end{aligned} \tag{3}$$

where $\hat{f}_\alpha$ denotes the spin-1 operator for component $\alpha \in \{x, y, z\}$ [51], μ_B is the Bohr magneton, $g_J \simeq 2$ is the Land g-factor and $\Delta E_{hf} = 2\pi\hbar \times 6.83$ GHz is the hyperfine splitting [44]. We note that B_x and thus ω_L, ω_Q may be time-dependent. Due to the $\hat{f}_x^2$ term the dynamics induced by the Hamiltonian involves both the vector 'spin orientation' components $\hat{f}_x, \hat{f}_y, \hat{f}_z$, and the rank-two tensor 'spin-alignment' components:

$$\hat{j}_{zx} \equiv \hat{f}_z\hat{f}_x + \hat{f}_x\hat{f}_z, \tag{4}$$

$$\hat{j}_{xy} \equiv \hat{f}_x\hat{f}_y + \hat{f}_y\hat{f}_x. \tag{5}$$

We find the single-atom equations of motion

$$\frac{\mathrm{d}}{\mathrm{d}t}\begin{pmatrix} f_x\\ f_y\\ f_z\\ j_{zx}\\ j_{xy}\end{pmatrix} = \begin{pmatrix} 0 & 0 & 0 & 0 & 0\\ 0 & 0 & -\omega_L & -\omega_Q & 0\\ 0 & \omega_L & 0 & 0 & \omega_Q\\ 0 & \omega_Q & 0 & 0 & \omega_L\\ 0 & 0 & -\omega_Q & -\omega_L & 0\end{pmatrix}\begin{pmatrix} f_x\\ f_y\\ f_z\\ j_{zx}\\ j_{xy}\end{pmatrix} \tag{6}$$

which describe a pair oscillators, $f_y - f_z$ and $j_{zx} - j_{xy}$, each with oscillation frequency ω_L, and mutual coupling frequency ω_Q.

In particular, according to equation (6) the z projection of the spin evolves as $f_z(t) = \cos(\omega_L t)\cos(\omega_Q t)$. That is, the quadratic Zeeman shift manifests as a modulation of the Larmor precession.

The collective spin of N condensed atoms is $\mathbf{F} \equiv \sum_{n=1}^{N}\mathbf{f}^{(n)}$, where the superscript indicates the nth atom. The dynamics of the collective spin then obeys

$$\hat{F}_i(t) = N(t)\hat{f}_i(t) \tag{7}$$

which describes the coherent oscillation of a macroscopic spin, and its decay caused by the loss of atoms.

We observe this dynamics by first preparing the condensate in the initial state $(1,0,0)^T$ (quantization axis along the B-field direction z), i.e. all the atoms in $m_F = +1$. We then ramp up the field component B_x, then ramp to zero B_z, leaving the field along x. This is done slowly compared to the Larmor frequency defined by the field amplitude, and the spins adiabatically follow the field and the quantization axis is always along the B-field. To rotate the spins to the y–z plane and form the state $\frac{1}{2}(1, \sqrt{2}, 1)^T$ (quantization axis along x), a $\pi/2$-RF pulse along y is applied. This starts the precession dynamics around the x axis. The spin polarization is tracked by performing non-destructive Faraday rotation measurements as described below.

5. Non-destructive probing of the spin polarization

We perform non-destructive Faraday rotation measurements of the spin state of the atoms, exploiting the spin-dependent interaction of a linearly polarized off-resonant beam with the vectorial component of the atomic polarizability, as described and shown in [52–55]. The interaction with the atoms causes the linear polarization of this beam to rotate and therefore to acquire a diagonal component, which is detected using a shot-noise limited polarimeter based on the differential photodetector (DFD) described in [56]. We have demonstrated the

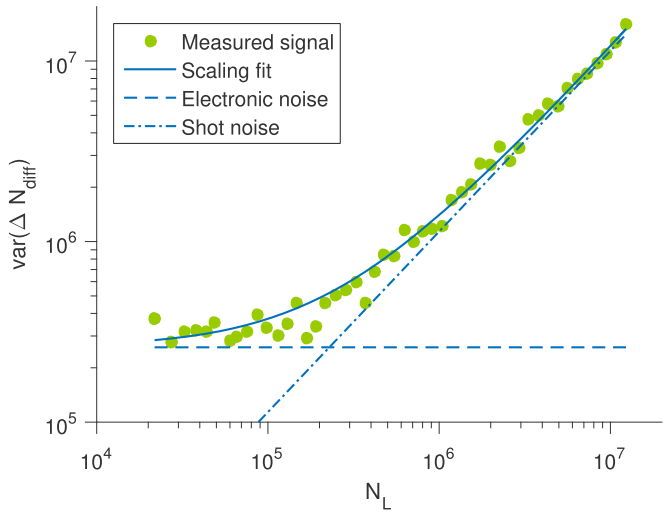

Figure 4. *Noise characterization of differential photodetector.* Variance of the output signal of the differential photodetector as a function of total input number of photons (N_L). The fit assumes the form $\mathrm{var}(\Delta N_{\mathrm{diff}}) = V_e + N_L$, the electronic noise floor corresponds to $V_e = 2.6(5) \times 10^5$ photons, and the linear region 2×10^5 to 10^7 photons is the shot-noise limited range.

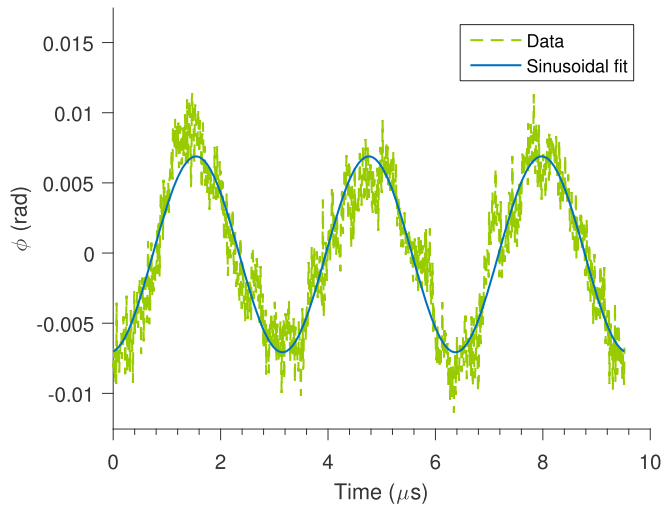

Figure 5. *Example of Faraday rotation signal.* We show the optical signal $\phi(t)$ of a continuous pulse containing 5×10^6 photons interacting with a fully polarized sample of atoms precessing around a magnetic field with Larmor frequency $\omega_L = 2\pi \cdot 300$ kHz. This signal is proportional to the projection of the atomic spin along the probing direction z, with proportionality constant $G_1 = 10^{-7}$ rad/spin such that $\phi(t) = G_1 F_z(t)$ (green line). We added a sinusoidal fit to the spin precession (blue line).

DFD is shot-noise limited for μs pulses with 2×10^5 to 10^7 photons, having an electronic noise floor equivalent to the shot noise of a pulse with $2.6(5) \times 10^5$ photons, as shown in figure 4.

The Faraday beam is red detuned 276 MHz from the $|F = 1\rangle \rightarrow |F' = 0\rangle$ transition and has linear polarization of 54.7° with respect to the bias field along x. At this 'magic angle' the tensorial ac-Stark shift averages to zero over one precession cycle [57], enabling continuous probing without conversion of spin alignment to spin orientation.

We perform continuous Faraday measurements that allow us to resolve a few Larmor cycles in a single pulse. This is typically performed using $\tau_p = 10$–20 μs pulses containing $N_L = 5 \times 10^6$ photons. To compensate probe power fluctuations, N_L is measured by splitting a fraction of the power to an auxiliary PD and transimpedance amplifier before entering the chamber. An example of the Faraday rotation signal is shown in figure 5. The polarization rotation angle in the Poincaré sphere $\phi = G_1 F_z$ is proportional to the collective spin component F_z, and with a coupling G_1 that depends on the overlap of the beam and the atomic cloud. For this reason, the probing beam is focused at the atoms position with a waist of 18 μm. For the pure condensate, we observe $G_1 = 10^{-7}$ rad/spin, by measuring the rotation angle caused by a fully polarized cloud with a known number of spins calibrated with absorption imaging.

The known shot-noise scaling of the optical angle allows us to estimate for one pulse with $N_L = 5 \times 10^6$ photons an optical angle noise of $\mathrm{d}\phi = 1/\sqrt{N_L} = 0.4$ mrad, which corresponds to an inferred noise in the spin state $(\sqrt{\mathrm{var}(F_z)})_{\mathrm{opt}} = (G_1\sqrt{N_L})^{-1} \simeq 4 \times 10^3$ spins. The noise is larger than the projection noise inherent to the atomic state, which is given by $(\sqrt{\mathrm{var}(F_z)})_{\mathrm{at}} = \sqrt{N} = 2 \times 10^2$ spins. The interaction with each pulse does not cause atoms to be lost from the trap, but it kicks atoms out from the condensate reducing the condensed fraction by 25%. Reaching projection noise limited measurements requires improvement to the coupling factor G_1 or the use of more photons if low damage is not required.

6. Magnetic coherence properties of the spinor BEC

To characterize the coherence properties of the macroscopic spin $\langle \mathbf{F}(t) \rangle$ of the single-domain SBEC, we use standard nomenclature [58] which identifies various relaxation times for different spin components, relaxation mechanisms, and scope of averaging. For a single-shot experiment with many spins (condensed or otherwise), the spin component along the field direction ($\mathbf{x}$), experiences the 'longitudinal' relaxation time $\mathcal{T}_1$, defined by $\langle F_x \rangle \propto \exp[-t/\mathcal{T}_1]$. Similarly, the transverse components, i.e., those orthogonal to the field direction, relax according to $\langle F_z \rangle_{\mathrm{hom}} \propto \cos[\Theta_L(t)]\exp[-t/\mathcal{T}_2]$ or $\langle F_z \rangle_{\mathrm{full}} \propto \cos[\Theta_L(t)]\exp[-t/\mathcal{T}_2^*]$ (and similar for $F_z \to F_y$, $\cos \to \sin$), where $\Theta_L(t) = \int_0^t \omega_L(t')\mathrm{d}t'$ is the accumulated precession angle. The averages $\langle\cdot\rangle_{\mathrm{hom}}$ and $\langle\cdot\rangle_{\mathrm{full}}$ indicate, respectively, averaging over only 'homogeneous' effects, i.e., irreversible randomizations affecting all spins in the same way, and averaging over both homogeneous effects and 'inhomogeneous' effects, i.e., apparent randomization due to reversible effects such as differences in the local field [59]. As concerns these single-shot relaxation times, the single-domain SBEC is expected to have $\mathcal{T}_2^* = \mathcal{T}_2 = \mathcal{T}_1$: In the SM approximation a single spin state $\hat{\mathbf{\Psi}}(t)$ describes the entire condensate, leaving no room for individual randomizations. There is in fact only one relaxation mechanism, loss of atoms, and this affects both F_x and $F_{y,z}$ in the same way, is truly irreversible, and affects all atoms in the same way. We assign the rate $1/\mathcal{T}_0$ to this loss of atoms: $N_A(t) \propto \exp[-t/\mathcal{T}_0]$.

Beyond these single-shot coherences, we must also account for the coherence of shot-to-shot averages. A change in the magnetic field between repetitions of the experiment generates $F_{y,z}(t)$ with a different phase Θ_L each time, and the average shows a relaxation-like behavior $\langle F_z \rangle_{\mathrm{ss}} \propto \langle \cos[\Theta_L(t)] \rangle_{\mathrm{ss}} \exp[-t/\mathcal{T}_2^*]$. In our system, as in most cold-atom experiments, $B_x(t)$ exhibits large variations implying large phase slips and a rapidly decaying average $\langle \cos[\Theta_L(t)] \rangle_{\mathrm{ss}}$. This decaying is only weakly related to the processes described by $\mathcal{T}_2^*$, and should be considered a characterization of the environment rather than of the SBEC itself.

Atom losses: Atom losses are caused by collisions with the background gas and by three-body collisions. The former knock condensate atoms out of the trap, or less frequently into the thermal cloud. The latter are strongly exothermic and result in loss of all three atoms. The atom number in the condensate evolves as

$$\dot{N} = -\frac{N}{\tau} - K_3 \int \mathrm{d}^3x\, n^3(x,\, t), \tag{8}$$

where the first term describes loss from background collisions and the second from three-body losses [60, 61]. For condensed atoms of ^{87}Rb , $K_3 \simeq 6 \times 10^{-30}$ cm^6 s^{-1} so that at our densities of $n \simeq 3 \times 10^{13}$ cm^{-3}, the three-body loss rate is of order $\simeq N/70$ s. In contrast, the observed number decay, measured by absorption imaging, is much faster, and well described by one-body losses with $\mathcal{T}_0 \equiv \tau = 7.7(4)$ s. The three-body loss can thus be neglected in these conditions.

Longitudinal spin relaxation: In the SD-SBEC the longitudinal macroscopic magnetization is conserved. Under the Hamiltonian of equation (3) above, both f_x and the magnetic quantum number m_F (in the x-basis) are constants of the motion, even for fluctuating $B_x(t)$. We confirm $\langle F_x(t) \rangle$ is also constant using Stern–Gerlach imaging to measure the population in the different magnetic sublevels as a function of hold time: a condensate is prepared in a stretched state $(1,\ 0,\ 0)^T$ or $(0,\ 0,\ 1)^T$ (quantization axes along $\mathbf{x}$) and held in the dipole trap during a time t_e, after which the atoms are released from the trap. During the time of flight a gradient field of $\sim$20 G cm^{-1} is applied for 10 ms to spatially separate the different spin components, before performing absorption imaging. The relative populations of the different spin states remain unchanged as a function of t_e, to within measurement precision, and therefore we identify $\mathcal{T}_1 = \mathcal{T}_0$.

We note that orthogonal ac magnetic fields at a frequency close to ω_L could resonantly excite transitions among m_F levels. The influence of such fields has limited the observation of spin dynamics in other experiments [45]. In our experiment this effect becomes evident only at bias fields below 100 mG.

Transverse spin relaxation: Shot-to-shot fluctuations of the field environment $B_{\mathrm{env}}(t)$ induce shot-to-shot decoherence on $\langle F_z(t) \rangle_{\mathrm{ss}}$ over different preparations. We characterize $B_{\mathrm{env}}(t)$ in our experiment as follows: using a three-axis fluxgate sensor (Mag-03 MCUP, Bartington) placed close to the vacuum cell, we measured the spectrum of environmental magnetic noise, which is dominated by the earth field (at dc), the mains frequency

Table 1. Measurement results of the magnetic field environment . The measurements were performed with a fluxgate sensor located 20 cm away from the atoms.

Mean amplitude (mG)	Standard deviation (μG)
$B_{\rm dc} = 451.5$	$\sigma_{\rm dc} = 200$
$B_{50} = 4.39$	$\sigma_{50} = 50$
$B_{150} = 2.09$	$\sigma_{150} = 20$

(at $\nu_{\rm mains} = 50$ Hz), and its third harmonic (at $3\nu_{\rm mains} = 150$ Hz), and is well approximated by the form: $B_{\rm env}(t) = B_{\rm dc} + B_1\cos(2\pi\nu_{\rm mains}t) + B_2\cos(3\cdot 2\pi\nu_{\rm mains}t)$. To estimate the fluctuations in the magnetic field environment in typical conditions, we measure the magnetic field at the cycle rate of the experiment (every 40 s), always after synchronizing with the mains cycle. The observations are summarized in table 1.

We then compute the average $\langle F_z(t)\rangle_{\rm ss}$ by Monte-Carlo simulation of 200 traces using equation (6) with B_x, given by $B_{\rm env}(t)$ where B_1 and B_2 drawn from normal distributions with the measured mean and standard deviation. $B_{\rm dc}$ is taken to be normally distributed with the measured standard deviation and a mean of 0.29 G, due to an applied offset field. This normal random noise defines a shot-to-shot decay rate $1/\overline{T_2}$, such that $\langle\cos[\Theta_L(t)]\rangle_{\rm ss} \sim \cos[\bar{\Theta}_L(t)]\exp[-t^2/\overline{T_2}^2]$, where $\bar{\Theta}_L = \langle\Theta_L(t)\rangle_{\rm ss}$. The amplitude of the $\langle F_z(t)\rangle_{\rm ss}$ oscillation decays with $\overline{T_2} \approx 1.5$ ms.

In a similar way we have estimated the magnetic field stability needed to have a stable phase Θ_L over different repetitions. $\overline{T_2}$ scales inversely with the field fluctuations and thus to increase it to the 1 s scale the field fluctuations must be reduced by a factor of ~1000, i.e., to the few pT level. While this is comparable to the noise of the fluxgate, small-volume atomic magnetometers [62] can have noise levels orders of magnitude below this, which may enable active cancellation to this level. Passive shielding of the chamber with a high-permeability enclosure can also provide such low-noise conditions [63].

To accurately measure the relevant property $\mathcal{T}_2^*$ of our spin system in the described magnetic environment, we take advantage of the non-destructive nature of the Faraday rotation probing, which allows us to probe several Larmor cycles of $F_z(t)$ during a single run and extract the amplitude via a sinusoidal fit. Because the amplitude does not depend on Θ_L, this allows meaningful averaging in spite of the shot-to-shot fluctuations. The quadratic phase Θ_Q also varies shot-to-shot, but on a time-scale about four orders of magnitude longer than does Θ_L, implying that the average amplitude will show effects of dephasing on the 10 s time scale.

We prepare the state $\frac{1}{2}(1,\ \sqrt{2},\ 1)^T$ and allow the atoms precess around the bias field $B_x = 0.29$ G for time t_e, before $F_z(t)$ is measured for 10 μs allowing several Larmor cycles to be resolved by fitting a sinusoidal function as in figure 5. We perform measurements at different values of t_e ranging from 0 to 1 s, each one on a new preparation of the state. The Larmor frequency is always ($\omega_L = 2\pi\cdot 200$ kHz). To separate the relaxation and decoherence signature from the atomic losses, we normalized the signal by the number of atoms measured by absorption imaging at the end of each repetition.

In figure 6 we plot the mean square amplitude of the sinusoidal fits for different repetitions, as a function of t_e. To these data we fit a function $A\cos^2(\omega_Q t)\exp(-2t/\mathcal{T})$, from which we find $\omega_Q = 2\pi\cdot 5.95(1)$ Hz as expected. As can be appreciated in the figure, the full visibility is always recovered and therefore $\mathcal{T} \gg 1$ s, much longer than the observation time.

To directly demonstrate the persistence of macroscopic spin precession, and thus of the magnetic coherence of the SD SBEC on longer timescales, we prepare an initial state $\frac{1}{\sqrt{2}}(1,\ 1,\ 0)^T$ by applying two MW pulses to the initial state $(1,0,0)^T$ (quantization axis along the magnetic field along x): a $\pi/2$ pulse resonant to the $|F=1,\ m_F=1\rangle \rightarrow |F=2,\ m_F=0\rangle$ transition followed by a π-pulse resonant to $|F=2,\ m_F=0\rangle \rightarrow |F=1,\ m_F=0\rangle$. We allow this state to precess before measuring its F_z polarization by Faraday rotation probing as described above. This state, in contrast to the fully polarized state $(1/2,1/\sqrt{2},\ 1/2)^T$, does not produce a modulation due to ω_Q, because only the 1, 0 coherence is non-zero. As a result, the single-atom polarization executes a pure oscillation $f_z(t) = -\frac{1}{\sqrt{2}}\cos(\omega_Q + \omega_L)t$. In figure 7 we show the amplitude of the Faraday signal and the number of atoms (measured by absorption imaging) as a function of the evolution time (t_e) up to 10 s. The decay of the amplitude is measured to be the same as the decay of the number of atoms, to within experimental uncertainty, this is $\mathcal{T}_2^* = \mathcal{T}_0$. In the insets we plot examples of the Faraday signal normalized by the number of atoms $\phi(t)/N(t_e) \propto \langle F_z(t)\rangle_{\rm full}/N(t_e)$. In these we observe the normalized amplitude is constant although the signal to noise decreases due to the loss of atoms.

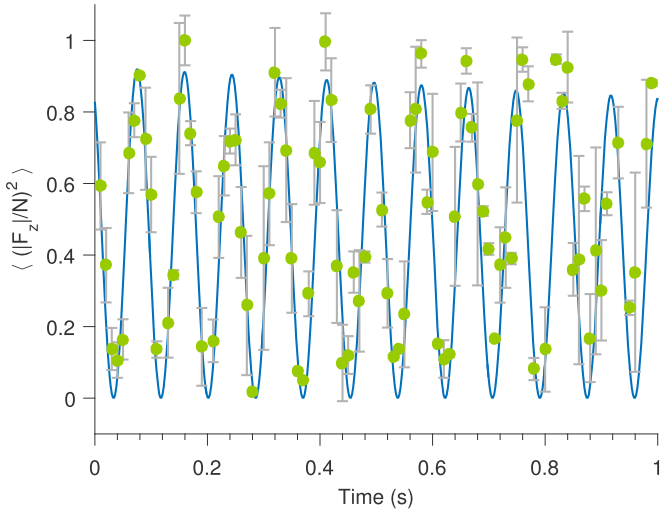

Figure 6. $\mathcal{T}_2^*$ measurement using a fully polarized state. Average over different repetitions of the squared of the magnitude of the z-component of the macroscopic spin (F_z) normalized by the number of atoms as a function of evolution time. Each repetition is obtained from the Faraday rotation measurements of a fully polarized condensate and the calibrated G_1. The spins rotate around x at Larmor precession frequency $\omega_L = 2\pi \cdot 200$ kHz. The amplitude modulation due to the quadratic component oscillates at $\omega_Q = 2\pi \cdot 5.95(1)$ Hz. We observe no measurable decay of the normalized magnetization, which implies $\mathcal{T}_2^* \gg 1$ s.

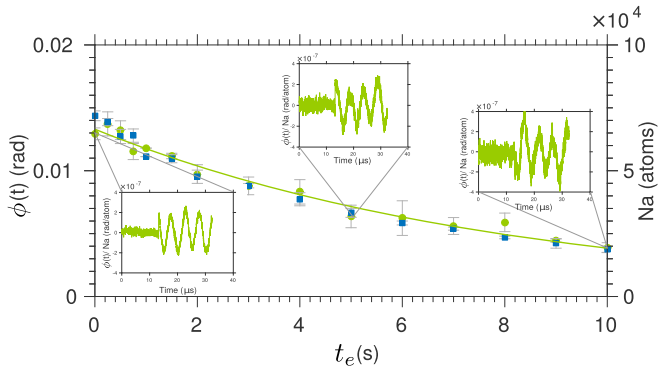

Figure 7. $\mathcal{T}_2^*$ measurement using an initial state $\psi(0) = (1,\ 1,\ 0)^T/\sqrt{2}$ (quantization axis along x). Amplitude of the Faraday signal (green circles, left axis) and number of atoms (blue squares, right axis) are shown versus evolution time (t_e). Green line shows best exponential fit to the amplitude data, with time constant 8.1(4) s (green line). A similar fit (not shown) to the number of atoms finds time constant 7.7(4) s, equal to within experimental uncertainty. Insets show examples of the Faraday signal, normalized by the number of atoms. These normalized amplitudes are equal over the 10 s observation time, showing no observable decoherence of the spin state. For these data $G_1 = -3.7 \times 10^{-7}$ rad/atoms.

Our results are consistent with the expectation of spin relaxation due solely to atom losses, which in our typical vacuum conditions is limited by one-body losses $\mathcal{T}_2^* \simeq \mathcal{T}_2 \simeq \mathcal{T}_1 \simeq \mathcal{T}_0 = 7.7(4)$ s.

7. Conclusions

We have described a system capable of creating SBECs of ^{87}Rb atoms in the ferromagnetic $F = 1$ hyperfine state. The experiment employs all-optical evaporation in a deep 1560 nm dipole trap, which we load by partially compensating the large induced differential light-shift using a 1529 nm laser. This allows us to benefit from both a high trap depth and a light-shift-induced dark MOT. We demonstrate non-destructive tracking of the macroscopic spin state using Faraday rotation probing.

Based on measurements of the spatial size, densities and coherence, we demonstrate the spinor condensate is created in a single spin domain. This SD spinor condensate behaves as a single large spin precessing around the magnetic field. We have observed collective spin precession with a single-shot coherence time of several seconds, limited only by the lifetime of the condensate, which is set by the vacuum conditions. Such extreme coherence properties are interesting for studies of atomic entanglement [23], macroscopic quantum states [24, 25], and non-locality in many-body systems [27]. Noting also the small size, the magnetic SM spinor condensate is

attractive for high-resolution field sensing [28, 29], with the possibility to attain sensitivities beyond the standard quantum limit [64, 65].

Acknowledgments

Work supported by European Research Council (ERC) projects AQUMET (280169) and ERIDIAN (713682); the Spanish MINECO projects MAQRO (Ref. FIS2015-68039-P), XPLICA (FIS2014-62181-EXP), the Severo Ochoa programme (SEV-2015-0522); Agència de Gestió d'Ajuts Universitaris i de Recerca (AGAUR) project (2014-SGR-1295); Fundació Privada CELLEX, and the Generalitat de Catalunya (CERCA Programme).

ORCID iDs

Silvana Palacios https://orcid.org/0000-0001-9479-2317
Simon Coop https://orcid.org/0000-0003-1538-3940
Morgan W Mitchell https://orcid.org/0000-0001-8949-9407

References

[1] Leanhardt A E, Shin Y, Kielpinski D, Pritchard D E and Ketterle W 2003 *Phys. Rev. Lett.* **90** 140403
[2] Choi J Y, Kwon W J and Shin Y I 2012 *Phys. Rev. Lett.* **108** 035301
[3] Ray M W, Ruokokoski E, Kandel S, Mottonen M and Hall D S 2014 *Nature* **505** 657–60
[4] Marti G E, MacRae A, Olf R, Lourette S, Fang F and Stamper-Kurn D M 2014 *Phys. Rev. Lett.* **113** 155302
[5] Sadler L E, Higbie J M, Leslie S R, Vengalattore M and Stamper-Kurn D M 2006 *Nature* **443** 312–5
[6] Scherer M, Lücke B, Gebreyesus G, Topic O, Deuretzbacher F, Ertmer W, Santos L, Arlt J J and Klempt C 2010 *Phys. Rev. Lett.* **105** 135302
[7] Stenger J, Inouye S, Stamper-Kurn D M, Miesner H-J, Chikkatur A P and Ketterle W 1998 *Nature* **396** 345–8
[8] Zhang W, Zhou D L, Chang M S, Chapman M S and You L 2005 *Phys. Rev. Lett.* **95** 180403
[9] Eto Y, Saito H and Hirano T 2014 *Phys. Rev. Lett.* **112** 185301
[10] Ho T L 1998 *Phys. Rev. Lett.* **81** 742
[11] Law C K, Pu H and Bigelow N P 1998 *Phys. Rev. Lett.* **81** 5257–61
[12] Yi S, Müstecaplıoğlu Ö E, Sun C P and You L 2002 *Phys. Rev.* A **66** 011601
[13] Lücke B *et al* 2011 *Science* **334** 773–6
[14] Gross C, Strobel H, Nicklas E, Zibold T, Bar-Gill N, Kurizki G and Oberthaler M K 2011 *Nature* **480** 219–23
[15] Hamley C D, Gerving C S, Hoang T M, Bookjans E M and Chapman M S 2012 *Nat. Phys.* **8** 305–8
[16] Hoang T M, Anquez M, Robbins B A, Yang X Y, Land B J, Hamley C D and Chapman M S 2016 *Nat. Commun.* **7** 11233
[17] Vengalattore M, Higbie J M, Leslie S R, Guzman J, Sadler L E and Stamper-Kurn D M 2007 *Phys. Rev. Lett.* **98** 200801
[18] Kronjäger J, Becker C, Brinkmann M, Walser R, Navez P, Bongs K and Sengstock K 2005 *Phys. Rev.* A **72** 063619
[19] Boyd M M, Zelevinsky T, Ludlow A D, Foreman S M, Blatt S, Ido T and Ye J 2006 *Science* **314** 1430–3
[20] Divincenzo D P 2005 *The Physical Implementation of Quantum Computation* (New York: Wiley) pp 1–13
[21] Zurek W H 2003 *Rev. Mod. Phys.* **75** 715–75
[22] Leibfried D, Blatt R, Monroe C and Wineland D 2003 *Rev. Mod. Phys.* **75** 281–324
[23] Riedel Max F, Böhi P, Li Y, Hänsch Theodor W, Sinatra A and Treutlein P 2010 *Nature* **464** 1170–3
[24] Beduini F A and Mitchell M W 2013 *Phys. Rev. Lett.* **111** 143601
[25] Beduini F A, Zielińska J A, Lucivero V G, de Icaza Astiz Y A and Mitchell M W 2015 *Phys. Rev. Lett.* **114** 120402
[26] Esteve J, Gross C, Weller A, Giovanazzi S and Oberthaler M K 2008 *Nature* **455** 1216–9
[27] Schmied R, Bancal J D, Allard B, Fadel M, Scarani V, Treutlein P and Sangouard N 2016 *Science* **352** 441–4
[28] Budker D and Romalis M 2007 *Nat. Phys.* **3** 227–34
[29] Muessel W, Strobel H, Linnemann D, Hume D B and Oberthaler M K 2014 *Phys. Rev. Lett.* **113** 103004
[30] Mercer L 1991 *J. Lightwave Technol.* **9** 485
[31] de Escobar Y N M, Álvarez S P, Coop S, Vanderbruggen T, Kaczmarek K T and Mitchell M W 2015 *Opt. Lett.* **40** 4731–4
[32] Appel J, MacRae A and Lvovsky A I 2009 *Meas. Sci. Technol.* **20** 055302
[33] Clément J F, Brantut J P, Robert-de Saint-Vincent M, Nyman R A, Aspect A, Bourdel T and Bouyer P 2009 *Phys. Rev.* A **79** 061406
[34] Bernon S, Vanderbruggen T, Kohlhaas R, Bertoldi A, Landragin A and Bouyer P 2011 *New J. Phys.* **13** 065021
[35] Olson A J, Niffenegger R J and Chen Y P 2013 *Phys. Rev.* A **87** 053613
[36] Friebel S, Scheunemann R, Walz J, Hänsch T and Weitz M 1998 *Appl. Phys.* B **67** 699–704
[37] Barrett M D, Sauer J A and Chapman M S 2001 *Phys. Rev. Lett.* **87** 010404
[38] Huang C Y, Chen C C, Sun L A, Liao G B, Wu K S, Lin Y J and Chang M S 2017 *J. Phys. B: At. Mol. Opt. Phys.* **50** 155302
[39] Coop S, Palacios S, Gomez P, de Escobar Y N M, Vanderbruggen T and Mitchell M W 2017 *Opt. Express* **25** 32550–9
[40] Reinaudi G, Lahaye T, Wang Z and Guéry-Odelin D 2007 *Opt. Lett.* **32** 3143–5
[41] Pethick C J and Smith H 2002 *Bose–Einstein Condensation in Dilute Gases* (Cambridge: Cambridge University Press)
[42] Stamper-Kurn D and Ketterle W 2001 Spinor condensates and light scattering from Bose–Einstein condensates *Coherent Atomic Matter Waves* (*Les Houches - Ecole d'Ete de Physique Theorique* vol 72) ed R Kaiser, C Westbrook and F David (Berlin: Springer) pp 139–217
[43] Kawaguchi Y and Ueda M 2012 *Phys. Rep.* **520** 253
[44] Stamper-Kurn D M and Ueda M 2013 *Rev. Mod. Phys.* **85** 1191–244
[45] Chang M S, Hamley C D, Barrett M D, Sauer J A, Fortier K M, Zhang W, You L and Chapman M S 2004 *Phys. Rev. Lett.* **92** 140403
[46] Schmaljohann H, Erhard M, Kronjäger J, Kottke M, van Staa S, Cacciapuoti L, Arlt J J, Bongs K and Sengstock K 2004 *Phys. Rev. Lett.* **92** 040402

[47] Chang M S, Qin Q, Zhang W, You L and Chapman Michael S 2005 *Nat. Phys.* **1** 111–6
[48] Kuwamoto T, Araki K, Eno T and Hirano T 2004 *Phys. Rev.* A **69** 063604
[49] He X, Zhu B, Li X, Wang F, Xu Z F and Wang D 2015 *Phys. Rev.* A **91** 033635
[50] Zhang W, Zhou D, Chang M S, Chapman M and You L 2005 *Phys. Rev.* A **72** 013602
[51] Colangelo G, Sewell R J, Behbood N, Ciurana F M, Triginer G and Mitchell M W 2013 *New J. Phys.* **15** 103007
[52] Higbie J M, Sadler L E, Inouye S, Chikkatur A P, Leslie S R, Moore K L, Savalli V and Stamper-Kurn D M 2005 *Phys. Rev. Lett.* **95** 050401
[53] Koschorreck M, Napolitano M, Dubost B and Mitchell M W 2010 *Phys. Rev. Lett.* **104** 093602
[54] Kaminski F, Kampel N S, Steenstrup M P H, Griesmaier A, Polzik E S and Müller J H 2012 *Eur. Phys. J.* D **66** 227
[55] Gajdacz M, Pedersen P L, Mørch T, Hilliard A J, Arlt J and Sherson J F 2013 *Rev. Sci. Instrum.* **84** 083105
[56] Ciurana F M, Colangelo G, Sewell R J and Mitchell M W 2016 *Opt. Lett.* **41** 2946–9
[57] Smith G A, Chaudhury S, Silberfarb A, Deutsch I H and Jessen P S 2004 *Phys. Rev. Lett.* **93** 163602
[58] Bloembergen N, Purcell E M and Pound R V 1948 *Phys. Rev.* **73** 679–712
[59] Abragam A 1961 *The Principles of Nuclear Magnetism* (Oxford: Oxford University Press)
[60] Burt E A, Ghrist R W, Myatt C J, Holland M J, Cornell E A and Wieman C E 1997 *Phys. Rev. Lett.* **79** 337–40
[61] Söding J, Guéry-Odelin D, Desbiolles P, Chevy F, Inamori H and Dalibard J 1999 *Appl. Phys.* B **69** 257–61
[62] Jiménez-Martínez R and Knappe S 2017 *Microfabricated Optically-Pumped Magnetometers* (Cham: Springer) pp 523–51
[63] Donley E A, Hodby E, Hollberg L and Kitching J 2007 *Rev. Sci. Instrum.* **78** 083102
[64] Sewell R J, Koschorreck M, Napolitano M, Dubost B, Behbood N and Mitchell M W 2012 *Phys. Rev. Lett.* **109** 253605
[65] Brask J B, Chaves R and Kołodyński J 2015 *Phys. Rev.* X **5** 031010